International Journal of Advanced Geosciences, 12 (1) (2024) 35-46

International Journal of Advanced Geosciences

Website: www.sciencepubco.com/index.php/IJAG

Research paper

Petrography and geochemistry of iron-bearing units from Mingo'o area (Ntem complex, southern Cameroon)

Rodrigue Edjo-Minko [1], Gbambie Isaac Bertrand Mbowou [1] *, Isaac Daama [2], Dagwai Nguihdama [3], Mike-Franck Mienlam Essi [4]

[1] *Department of Mines and Geology, School of Geology and Mining Engineering, University of Ngaoundere, PO. Box 115, Meiganga, Cameroon*
[2] *Department of Petroleum and Gas Engeineering, School of Geology and Mining Engineering, University of Ngaoundere, PO. Box 115, Meiganga, Cameroon*
[3] *Department of Earth Sciences, Faculty of Sciences, University of Maroua, P.O. Box 46 Maroua, Cameroon*
[4] *Department of Geoscience and Environment, University of Ebolowa, P.O. Box 118 Ebolowa, Cameroon*
**Corresponding author E-mail: mbowou2000@yahoo.fr*

Abstract

The banded iron formation (BIF) of the Mingo'o region is located on the northern edge of the Congo Craton. They constitute a significant component of the southern Cameroonian Archean to Paleoproterozoic. Petrographic description indicates that the most characteristic facies of the Mingo'o BIFs are quartz-magnetite BIFs (QMB), which are mostly composed of magnetite and quartz. Geochemistry analyses show that the major elements of this BIF are very simple, with SiO_2 and Fe_2O_3 representing 95.25 wt. % of the bulk rock on average. The low concentrations of Al_2O_3, TiO_2, and HFSE reveal that these chemical sediments are detritus-free. According to Paerson's major element correlation matrix, there is a slight contribution of detrital material to chemical sediment, as confirmed by the strong positive correlation ($r = 0.72$) of Al and Ti, also by the binary diagrams Al vs. $\Sigma(Y + Nb + Zr)$ with a weak positive correlation ($r^2 = 0.31$) and Al vs. ΣREE with a zero correlation ($r^2 = 0.08$), indicating that the detrital input was insignificant. The transition metals Zn, Cr, Sr, and V are among the trace elements with low enrichments. This suggests the direction of the volcanogenic hydrothermal input in chemical precipitates. The mean ∑REE concentration of the studied BIF is 26.74 ppm, with a range of 8.82 to 36.74 ppm. Pure chemical sediments are comparable to that. The shale-normalized patterns display minor positive europium anomalies, a sharp decrease in heavy REE, and enrichment in light REE. These geochemical characteristics suggest that the hydrothermal activity in the deep ocean, coupled with seawater, was the source of the Fe and Si. Low-temperature hydrothermal solutions play a key role in the studied BIF, as shown by the absence of a notable positive Eu anomaly. Ce anomalies are seen in the chrondrite-normalized REE patterns, which are characterized by LREE-enriched (mean $La_{CN}/Yb_{CN} = 5.28$) and HREE depletion (mean $Tb_{CN}/Yb_{CN} = 1.04$) patterns. This may indicate that the BIF within the Mingo'o region was formed in place of the basin towards redoxcline, alternating at different times and under various influences from the influx of seawater that has been oxidized.

Keywords: *Banded Iron Formations; Congo Craton; Hydrothermal Fluids; Seawater.*

1. Introduction

Sedimentary rocks with a Fe content of 15% or above compose the majority of the stratigraphic units identified as the Iron Formations (IFs) [1,2]. Due to interpreted depositional circumstances [3,4], IFs have historically been divided into two types: superior type and algoma type. Superior-type of IFs are commonly found interbedded with carbonates, quartz arenite, and black shale; it is assumed that they were deposited in nearshore continental shelf environments. Algoma-type of IFs can occur in graywacke but are more frequently seen in volcanic rocks. It is believed that exhalative-hydrothermal processes produced them close to volcanic centers [4]. Based on their textural features, two groups of iron formations (IFs) can be identified: banded iron formations (BIFs) and granular iron formations (GIFs) [5–7].
Despite the importance of iron's everyday use in meeting human requirements, iron production continues to attract attention on a global scale [8]. Moreover, significant advancements in iron exploration have been achieved by mining countries such as Australia, Brazil, and South Africa [9–12]. In South Africa, [9] show the origin and palaeoenvironmental significance of major iron formations at the Archean-Paleoproterozoic boundary. Very little progress has been achieved in Cameroon's iron mineralization research, despite several studies and discoveries by academics and mining companies. This is occurring in southern Cameroon, especially in the areas of Mbalam, Mamelles, Nkout, Ngovayang, Meyongo, and Mayo-Binka in the Ntem Complex, on the northern edge of the Congo Craton [13–22]. But because the origin of iron mineralization still has to be determined, there are still some places where the search for iron mineralization has not yet advanced. This is currently the case under investigation at the northern edge of the Congo Craton, in the Mingo'o region of southern Cameroon. Therefore, in order to expand iron exploration both globally and in Cameroon specifically, the objective of this study is to determine the origin of Mingo'o's iron mineralization using petrographic and geochemical data.

2. Geological setting

2.1. Regional geology

The northern edge of the Congo Craton in Cameroon constitutes the Ntem complex [23], [24] (Fig. 1a). The Pan-African orogenic belt, which is a relatively stable block of Archean and Palaeoproterozoic rocks, covers this complex from the north [25], [26]. Over a distance of more than 500 kilometers, the Ntem complex is separated into three main units: the eastward-facing Ayna unit, the central Ntem unit, and the westward-facing Nyong unit (Fig. 1b).

Greenstone belts, a banded series, and an intrusive series are formations that define the Ntem unit (Fig. 1b). The bulk of the intrusive series is located in the northern area and is composed of the magmatic Charnockitic suite and the Tonalite-Trondjemite-Granodiorite (TTG) suite [23], [27]. Among the significantly deformed granulitic gneisses that comprise the banded series are leptynites, enderbergites, granitic gneisses, and charnockitic gneisses, which are distributed across the southern part of the Ntem unit [23], [28]. The fractured bands and xenoliths of greenstones from the Ntem unit are discovered in the intrusive series, indicating that they formed earlier BIFs. These supra-crustal rocks are composed of metagraywackes, paragneisses containing sillimanite, amphibolites having garnet, and pyroxenites [29]. They experienced granulite-facies metamorphism with estimated peak temperatures of 750 ± 50 °C at 5–6 kbar [26]. The location of the greenstone belts in the Ntem unit has been dated to about 3.1 Ga using the zircon Pb-Pb evaporation process [30]. Greenstone belts are seriously fragmented by late syenitic plutons and doleritic veins that crosscut them [26].

The rocks of the Ayna unit (Fig. 1b) are the same as those of the Ntem unit. This unit is associated with a Paleoproterozoic trench composed of the volcano-sedimentary Mbalam series. Granodiorites are also present in this region. The volcano-sedimentary sequence gneissified between 2 and 2.1 Ga, forming Eburnian granodiorites. Liberian N130°E foliation continued after massive senestial N40°E blastomylonite gullies and posterior N50°E folds ascribed to the Eburnian orogeny [23].

The Nyong unit, which involves Mingo'o iron mineralization (Fig. 1b), was reworked as part of the northern edge of the Congo Craton in Cameroon during the Eburnian-Transamazonian orogeny [24], [31], [32]. It is composed of iron-rich formations, mafic and ultramafic metavolcanics, migmatitic grey gneisses of TTG composition, syn to late tectonic charnockites, augenic metadiorites, orthopyroxene gneiss, amphibolo-pyroxenites, garnet-rich gneisses, and granites [31], [32]. In the polycyclic metamorphic of the high-grade gneisses of the Nyong unit, Pan-African high-grade recrystallization overprints the Paleoproterozoic granulite assemblage [31], [33]. Recent examples of eclogite facies metamorphic rocks include garnet-clinopyroxenites and garnet-clinopyroxene amphibolites found in the high-grade supracrustal gneisses of the Nyong Range [34], [35]. These rocks belong to the Nyong unit greenstone formation. According to [36], their pressure-temperature conditions of around 25 kbar and 850 °C suggest that they were buried at a depth of more than 90 km and with a lower geothermal gradient of roughly 10 °C/km. The metamorphism of the eclogite facies is limited to 2.09 Ga by eclogite samples from SHRIMP U-Pb analysis [35]. Massive local open folds generally connected to N-S sinister sliding faults, a shallow to moderately dipping S1/S2 regional trough, and a variably oriented stretching lineation are the components that define the Nyong unit. The highest depositional age for the Nyong unit, as determined by SHRIMP U-Pb studies, is 2423 ± 4 Ma [31].

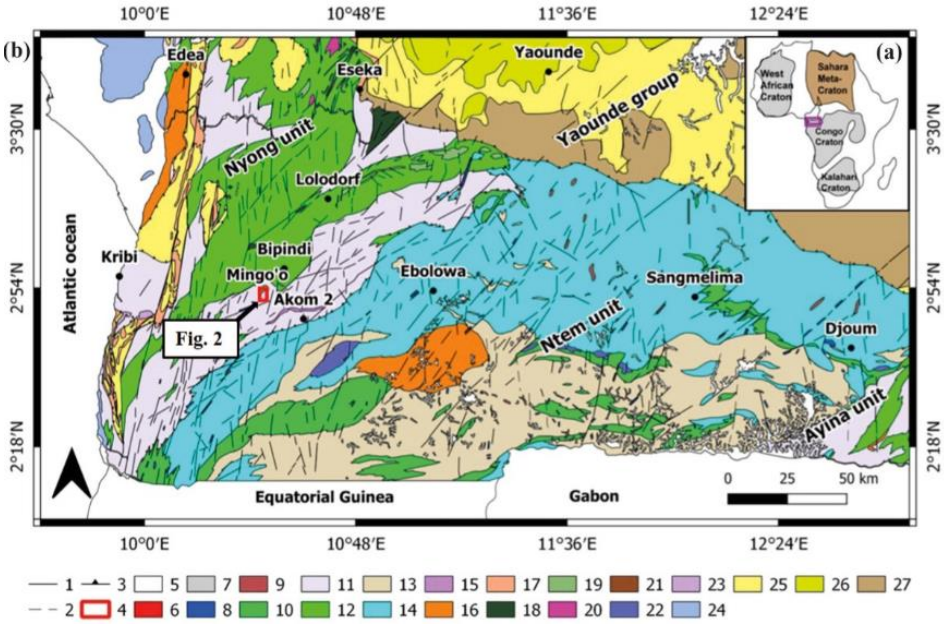

Fig. 1: (A) - Craton Map in Africa. (B) - Geological Map Of South West Cameroon Modified From [23]: 1. Faults, 2. Supposed Faults, 3. Overlaps, 4. Study Area, 5. Quaternary Fluvial and Coastal Deposits, 6. Itabirites Quartzites from the Neoarchean to the Paleoproterozoic, 7. Ultrabasites, Veins Rocks, 8. Dolerites, Veins Rocks, 9. Gabbros, Veins Rocks, 10. Archean Noritic Gneiss, 11. Paleoproterozoic Neoarchean Garnetiferous Amphibolitic Gneiss, 12. Amphibolites, Garnetites, Eclogitoids from the Neoarchean to the Paleoproterozoic, 13. Archean Granulitic Gneisses, Leptynites, Enderbites, 14. Archean Charnockitic Grainy Core, 15. Archean Syenite Charnockites, 16. Porphyroid Biotite-Amphibole Granites, 17. Micaceous Quartzites of the Yaounde Group, 18. Neoarchean To Paleoproterozoic Tonalites, 19. Neoarchean to Paleopraoterozoic Nepheline Syenites, 20. Undifferentiated Neoarchean To Paleoproterozoic Granites. 21. Neoarchean to Paleoproterozoic Amphibole Granites, 22. Archean Leucocratic, Biotite and Alaskitic Granites, 23. Neoarchean to Paleoproterozoic Nepheline Syenites, 24. Sedimentary Pile of the Post Panafrican Cover, 25. Schist, Limestone of the Neoproterozoic, 26. Two-Mica Gneiss, Anatectites of Yaounde Group, 27. Muscovite-Chlorite Quartzitic Epischists of Yaounde Group.

2.2. Local geology

Paleoproterozoic Neoarchean garnetiferous amphibolitic rocks constitute the Mingo'o region [23]. In addition, we discover banded iron formations, amphibolites, and amphibole garnet gneiss (Fig. 2). Their outcrops frequently take the shape of stable domes, massively stuctured slabs and blocks, and microlithic textures with granular or semi-granular textures. BIFs are composed of 0.5 to 1.5 cm-long meso-bands of Fe-oxide and recrystallized quartz that alternate in a dynamic pattern and change from greenschist to amphibolite facies. But transposition and metamorphic differentiation have destroyed it, resulting in the formation of tectonometamorphic layers of iron oxides and quartz. Itabirite's layered structure is usually inherited from the parent sediment, which is rich in iron. The principal directions in the area are similar to NE-SW and NE-SSW, according to an analysis of remote sensing data.

3. Sampling and analysis methods

Eight representative BIF samples were chosen for petrographic and geochemical analysis in this study. In Figure 2, the sample sites are represented. The Institut for Geological and Mining Research (Cameroon) Ore Processing Laboratory generated polished thin sections. Polarizing microscopy was used in the Laboratory of the School of Geology and Mining Engineering, University of Ngaoundere (Cameroon), to carry out petrographic studies of these thin sections. Geochemical analysis was done using the pulp. Whole-rock analyses were done by Inductively Coupled Plasma-Atomic Emission (ICP-AES) for major elements and by Inductively Coupled Plasma Mass Spectrometry (ICP-MS) for trace elements at ALS Global, Brisbane (Australia). The samples were pulverized to obtain a homogeneous sample, out of which 50–60 g were obtained for the analyses. 0.1 g of rock powder was fused with 1.5 g of $LiBO_2$ and then dissolved in 100 mm^3 of 5% HNO_3. Loss on ignition (LOI) was determined by the weight difference after ignition at 1025 °C. Various standards were used, and data quality assurance was verified by running these standards between samples as unknowns.

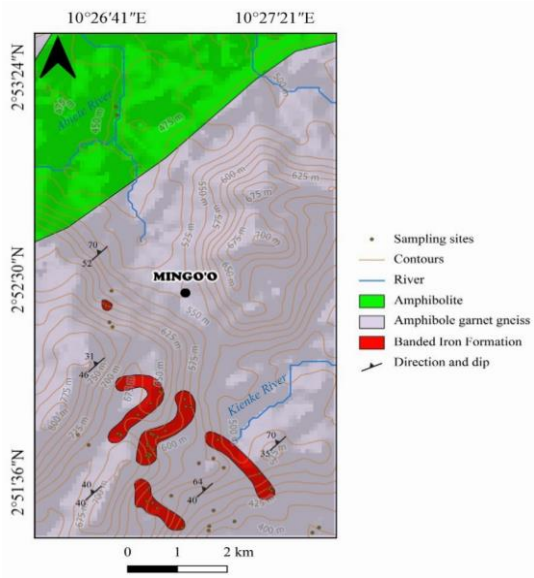

Fig. 2: Geological Map of the Mingo'o Area.

4. Results

4.1. Petrography

The banded iron formations observed are represented by one type of facies, which is quartz-magnetite BIFs (QMB). This facies is the most representative.

4.1.1. Quartz-magnetite BIFs

It is dispersed throughout the soil in the form of blocks (Figs 3a and b). They are available in two different color varieties: Fig. 3c shows a reddish-grey color with good compositional bedding, and Fig. 3d illustrates a gray color with fine bedding that alternates between light and dark levels. The light and dark minerals alternate continuously throughout this rubbing. The light minerals have a millimeter thickness and a quartzo-feldspathic composition. Magnetite makes up the majority of the dark minerals (Figs 3e and f).

The rock has a granolepidoblastic texture in thin sections (Figs 3e and f). Its main constituents are quartz (30–35 vol.%), potassium feldspar (5–10 vol.%), and magnetite (50–55 vol.%).

The most common iron mineral is magnetite, which may be found in bands that are Si-rich at percentages under 30 vol. % and Fe-rich at percentages over 50 vol. %. Black magnetite crystals in both bands range in size from 0.1 to 2 mm and have subhedral to anhedral shapes (Figs 3e and f). Magnetite crystals can occur alone in quartz grains or in clusters to create asymmetric aggregates (Figs 3e and f). There are quartz and feldspar inclusions in some magnetite grains (Figs 3e and f).

In the Si-rich bands, quartz predominates as subhedral to anhedral crystals with diameters ranging from 0.1 to 2 mm. Within the Fe-rich bands, quartz crystals often occur as amorphous aggregates rather than as discrete grains. In general, quartz combines with feldspar to create elongated polycrystalline bands, which are transparent beds that match the light beds of the rock. It is also xenomorphic (Figs 3e and f).

K-feldspar crystals range in size from 0.1 to 0.5 mm and appear in xenomorphic crystal forms. There are spots on these crystals where weathering has occurred (Figs 3e and f).

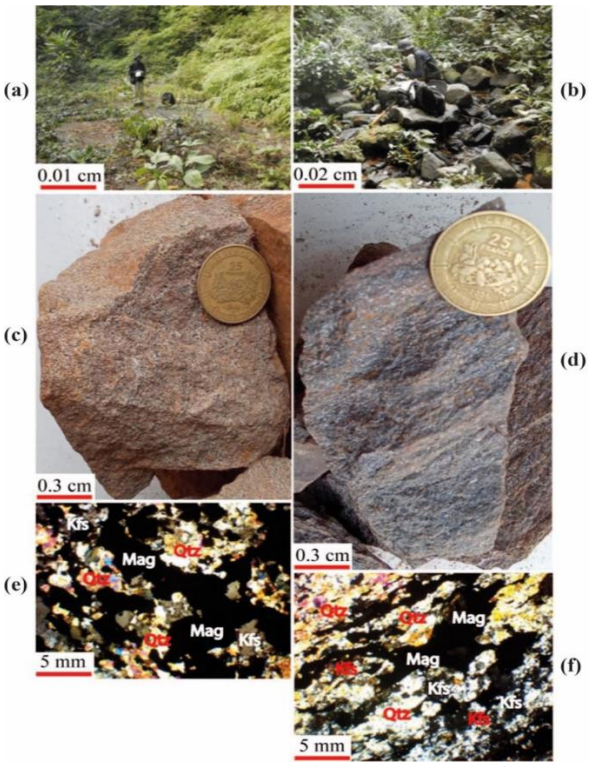

Fig. 3: (A), (B), (C), (D), (E), And (F) - Macroscopic and Microscopic Views of the Iron Fomations of the Studied Locality: Quartz-Magnetite Bifs (QMB).

4.2. Geochemistry

4.2.1. Major elements

Table 1 displays the major elements of the overall geochemical composition of eight representative samples from the Mingo'o banded iron formations. These iron formations have basic element chemistry, with SiO_2 and Fe_2O_3 as the main components (all Fe being expressed as Fe^{3+}). This is evident from the petrography and the general mineralogy of the rocks under study, which are mostly composed of quartz and iron oxide/hydroxyl minerals. The table shows that Fe_2O_3 is the most abundant major oxide in all samples, with values ranging from 49.5 to 73.7 wt. % (mean: 60.95 wt. %), resulting in a percentage of native iron that varies from 34.62 to 51.54 wt. %. The second is SiO_2, with values ranging from 15.25 to 44.3 wt. % (mean: 34.29 wt. %). SiO_2 and Fe_2O_3 make up an average of 95.25 wt. % of the mass of the banded iron formations. Samples MIN3 and MIN21 are marked by high concentrations of Fe_2O_3 (73.7 wt. %, respectively) and low concentrations of SiO_2 (15.25 and 16.95 wt. %, respectively), showing, compared with the other samples, high signs of weathering of SiO_2 in favor of Fe_2O_3.

In the respective binary diagrams (Fig. 4): SiO_2/Fe_2O_3 (r^2 = 0.888), K_2O/Fe_2O_3 (r^2 = 0.431), TiO_2/Fe_2O_3 (r^2 = 0.006), CaO/Fe_2O_3 (r^2 = 0.064), MnO/Fe_2O_3 (r^2 = 0.46), MgO/Fe_2O_3 (r^2 = 0.603), and Na_2O/Fe_2O_3 (r^2 = 0.509), we observe negative correlations (Figs 4a, b, d, e, f, g and i), which show progressive decreases of SiO_2, K_2O, TiO_2, CaO, MnO, MgO, and Na_2O, while Fe_2O_3 increases. A positive correlation is observed in the binary diagrams Al_2O_3/Fe_2O_3 (r^2 = 0.579) and P_2O_5/Fe_2O_3 (r^2 = 0.555), showing the progressive increase of Al_2O_3 and P_2O_5 with Fe_2O_3 (Figs 4c and h). The Pearson correlation matrix (Table 2) confirms the binary diagrams obtained. It shows that there is a strong negative correlation (r = -0.94) between Fe_2O_3 and SiO_2 in different mineral phases. Al_2O_3 shows a negative correlation with SiO_2 (r = -0.49) and a positive correlation with Fe_2O_3 (r = -0.25). CaO, MgO, Na_2O, K_2O, TiO_2, and MnO show negative correlations with Fe_2O_3 (r = -0.76, r = -0.78, r = -0.71, r = -0.66, r = -0.08, and r = -0.68, respectively), while P_2O_5 shows a positive correlation with Fe_2O_3 (r = 0.75).

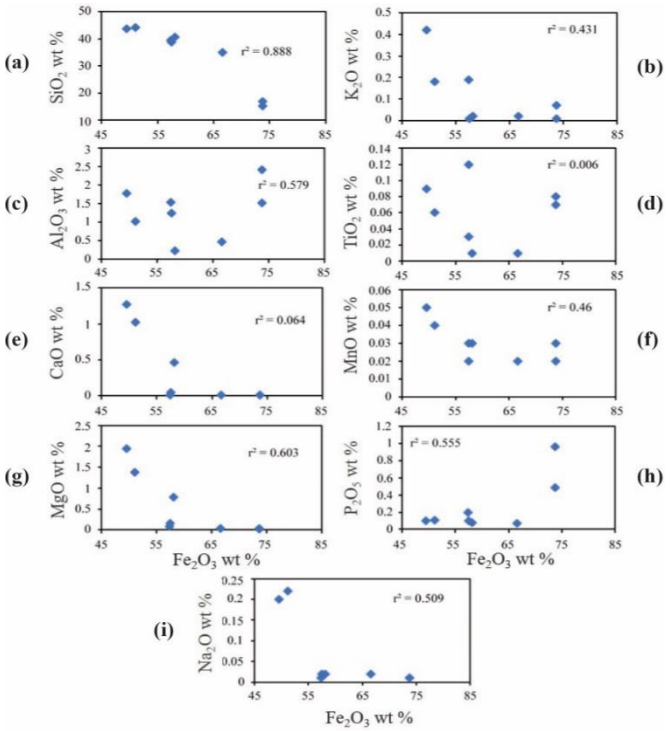

Fig. 4: Binary Diagrams of Major Element Variations as A Function of Fe_2O_3: (A) - Sio_2/Fe_2O_3; (B) - K_2O/Fe_2O_3; (C) - Al_2O_3/Fe_2O_3; (D) - Tio_2/Fe_2O_3; (E) - Cao/Fe_2O_3; (F) - Mno/Fe_2O_3; (G) - Mno/Fe_2O_3; (H) - P_2O_5/Fe_2O_3; (I) - Na_2O/Fe_2O_3.

Table 1: Major Element Composition (Wt. %) and Element Ratios of the Mingo'o BIF

Sample	MIN3	MIN4	MIN7	MIN10	MIN12	MIN17	MIN18	MIN21	Mean
Weight percent (wt %)									
SiO_2	15.25	38.90	35.00	39.50	43.70	44.30	40.70	16.95	34.29
Al_2O_3	1.52	1.24	0.47	1.54	1.79	1.03	0.23	2.42	1.28
Fe_2O_3	73.70	57.50	66.60	57.40	49.50	51.10	58.10	73.70	60.95
CaO	0.01	0.05	0.01	0.01	1.27	1.02	0.46	0.01	0.36
MgO	0.02	0.15	0.03	0.08	1.94	1.38	0.78	0.03	0.55
Na_2O	0.01	0.02	0.02	0.01	0.20	0.22	0.02	0.01	0.06
K_2O	0.01	0.01	0.02	0.19	0.42	0.18	0.02	0.07	0.12
TiO_2	0.08	0.03	0.01	0.12	0.09	0.06	0.01	0.07	0.06
MnO	0.03	0.02	0.02	0.03	0.05	0.04	0.03	0.02	0.03
P_2O_5	0.96	0.10	0.07	0.20	0.10	0.11	0.08	0.49	0.26
LOI	6.04	0.31	-0.81	1.06	-0.40	-1.48	-0.36	5.87	1.28
Total	97.63	98.33	101.44	100.14	98.66	97.96	100.07	99.64	99.23
Fe	51.54	40.21	46.58	40.14	34.62	35.73	40.63	51.54	42.62
Si/Al	8.90	27.97	68.13	22.79	21.72	38.33	158.50	6.19	44.07
Fe/Al	64.07	61.28	187.28	49.25	36.55	65.55	333.81	40.24	104.75
Al/Ti	20.00	65.00	48.00	11.57	18.80	18.00	24.00	32.00	29.67
Fe/Ti	1288.50	4021.00	9316.00	573.43	692.40	1191.00	8126.00	1288.50	3312.10

Table 2: Pearson's Correlation Matrix for Major Element Oxides

	SiO_2	Al_2O_3	Fe_2O_3	CaO	MgO	Na_2O	K_2O	TiO_2	MnO	P_2O_5	LOI
SiO_2	1.00										
Al_2O_3	-0.49	1.00									
Fe_2O_3	-0.94	0.25	1.00								
CaO	0.60	-0.03	-0.76	1.00							
MgO	0.62	-0.04	-0.78	1.00	1.00						
Na_2O	0.55	0.06	-0.71	0.94	0.91	1.00					
K_2O	0.47	0.37	-0.66	0.78	0.79	0.75	1.00				
TiO_2	-0.14	0.72	-0.08	0.12	0.12	0.20	0.60	1.00			
MnO	0.47	0.09	-0.68	0.90	0.91	0.84	0.85	0.44	1.00		
P_2O_5	-0.89	0.46	0.75	-0.40	-0.42	-0.35	-0.30	0.36	-0.15	1.00	
LOI	-0.96	0.65	0.83	-0.53	-0.54	-0.50	-0.32	0.36	-0.34	0.91	1.00

4.2.2. Trace elements

The trace element contents of the whole rock in the Mingo'o BIF samples are displayed in Table 3. When compared to the composition of the upper continental crust, the concentrations of trace elements, such as high-field elements (HFSE), transition trace metals, and rare earth elements, are relatively low (Fig. 5; [37], [38]). It should be noted that trace element concentrations are frequently low, as is the case with other BIFs across the world [9,39]. Transition metals such as Zn (20–101 ppm), Cr (7–91 ppm), Sr (1.4–8.3 ppm), and V (10–39 ppm) are examples of trace elements with low enrichment. These elements (Zn, Cr, Sr, and V) are commonly used as indicators of direct hydrothermal input from volcanoes in chemical precipitates, according to [40], [41]. [42], [43] reveal that whereas Zr, Hf, Rb, Y, and Sr are frequently generated from the alteration of felsic rocks in the Earth's crust, Cr, Ni, Co, V, and Sc have a mafic source. When compared to the upper continental crust, incompatible elements such as Th (0.500 ppm), Hf (0.227 ppm), Sc (5.875 ppm), and Zr (8.000 ppm) are discovered in very low concentrations. This suggests that there is little to no detrital origin for the silicates [44].

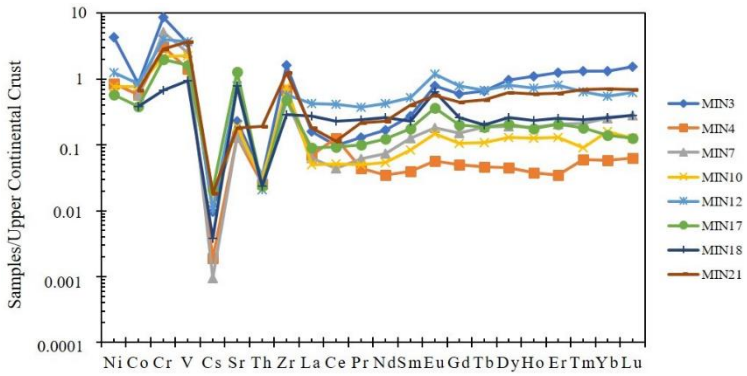

Fig. 5: Trace Elemental Patterns of the Mingo'o Iron Formations.

4.2.3. Rare earth elements

All of the BIF samples had a total REE concentration ranging from 8.82 to 66.54 ppm. When comparing nearly flat or slightly fractionated HREE ($(Tb/Yb)_{CN}$ = 0.61-1.65 ppm) to REE profiles normalized with the chrondrite (CN index, [37,38]), enrichment in LREE ($(La/Yb)_{CN}$ = 1.11-10.92 ppm) is evident, just like the negative to positive anomalies in Eu ($(Eu/Eu^*)_{CN}$ = 0.46-1.87 ppm) (Table 3 and Fig. 6a). This suggests a low-rare earth fractionation. In comparison to HREE ($(Tb/Yb)_{SN}$ = 0.52-1.41 ppm), the REE profiles normalized to the post-Archean Australian shales (PAAS, SN index, [37], [38]) similarly demonstrate enrichment in LREE ($(La/Yb)_{SN}$ = 1.64-16.15 ppm), but with positive Eu anomalies ($(Eu/Eu^*)_{SN}$ = 1.27-2.61 ppm) and negative to positive anomalies in Ce ($(Ce/Ce^*)_{SN}$ = 0.63-2.17 ppm) (Table 3 and Fig. 6b). The Figure 7 displays the $(Ce/Ce^*)_{SN}$ vs. $(Pr/Pr^*)_{SN}$ diagram introduced by [45]. This diagram allows us to differentiate between real and false Ce anomalies in iron formations that may be caused by anomalous La abundances. In this diagram (Fig. 7), only one sample is in field I (no Ce or La anomaly), while three samples are in field IIa (positive La anomaly) and two others are in field IIIb (true negative Ce anomaly).

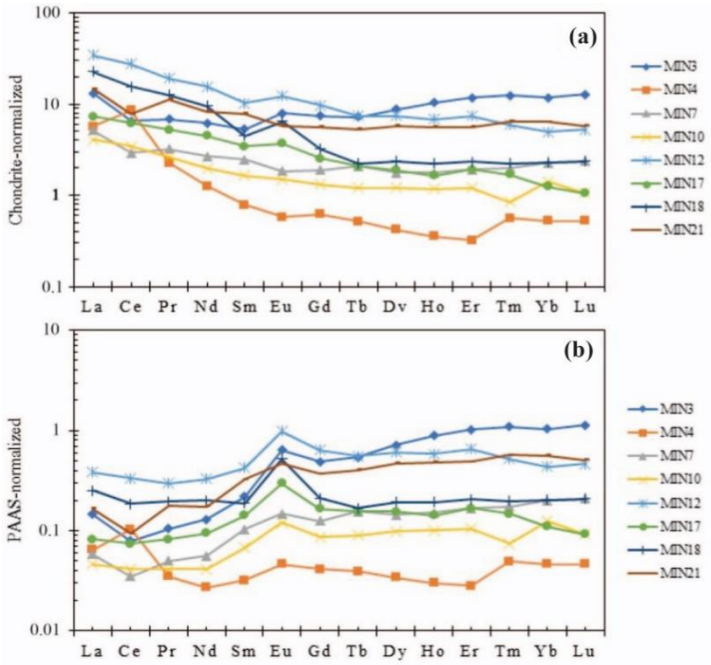

Fig. 6: (A) - Chondrite-Normalized; (B) - PAAS-REE Patterns of Mingo'o BIF. Normalization Value of PAAS and Chondrite After [37], [38].

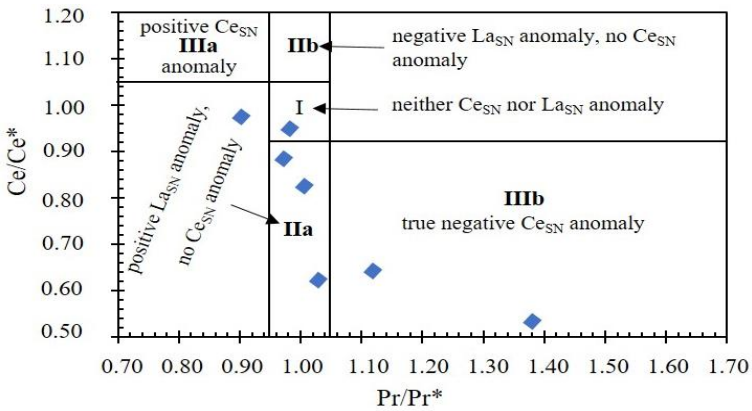

Fig. 7: $(Ce/Ce^*)_{SN}$ Vs. $(Pr/Pr^*)_{SN}$ Diagram After [45] for the Mingo'o BIF.

5. Discussion

5.1. Source of the chemical component

It was initially proposed by [5], [46] that the primary constituents of BIFs, silica and iron, originated from seawater. The origins of Fe and Si, according to [39], [47], are considered to be deep ocean hydrothermal activity combined with seawater. This theory explains why nearly all BIFs' REE profiles have positive Eu anomalies [48]. The Mingo'o BIFs' chemical composition shows that SiO_2 and Fe_2O_3 constitute the majority of the composition, with lower proportions of Al_2O_3, TiO_2, MnO, MgO, and CaO following (Table 1). The purity of the chemical precipitates is shown by the high concentrations of SiO_2 and Fe_2O_3 found in the banded iron formations studied. Al_2O_3 and TiO_2 are regularly used as indicators of clastic input, whereas Fe and Mn operate as partial hydrothermal proxies [40,49]. Terrigenous clastic materials were involved in the deposition of the Mingo'o BIFs, as shown by the strong positive correlation of Al with Ti and K (Table 3, [50], [51]). Nonetheless, the samples studied reveal a heterogeneous distribution (nugget effect) in the binary diagrams Al vs. Σ(Y + Nb + Zr) and Al vs. ΣREE (Figs 8a and b), indicating that the detrital input was insignificant. Furthermore, there is a low detrital input during the precipitation of BIFs, illustrated by the concentrations of HFSE (such as Nb, Zr, Hf, U, Th, and Pb) that are normally enriched in chemically developed crusts [41]. The foregoing signatures all suggest the insignificant contribution of crustal materials to the chemical precipitation of the BIFs studied.

Table 3: Trace and Rare Earth Element Compositions (Ppm) and Element Ratios of BIF From Mingo'o Area

Sample	MIN3	MIN4	MIN7	MIN10	MIN12	MIN17	MIN18	MIN21	Mean
Parts per million (ppm)									
Zn	101.000	66.000	42.000	54.000	53.000	57.000	20.000	48.000	55.125
Cu	23.000	17.000	12.000	17.000	3.000	3.000	2.000	27.000	13.000
Ni	45.000	9.000	<dl	8.000	13.000	6.000	<dl	<dl	10.125
Co	9.000	6.000	6.000	8.000	9.000	4.000	4.000	7.000	6.625
Cr	91.000	32.000	54.000	23.000	42.000	21.000	7.000	30.000	37.500
V	37.000	15.000	26.000	24.000	39.000	17.000	10.000	39.000	25.875
Nb	0.950	1.040	0.290	0.740	0.980	0.460	0.170	1.800	0.804
Cs	0.100	0.020	0.010	0.160	0.110	0.220	0.040	0.190	0.106
Hf	0.310	0.210	0.130	0.240	0.270	0.180	0.080	0.390	0.227
Sc	5.000	11.000	4.000	4.000	5.000	1.000	<dl	17.000	5.875
Rb	0.800	0.400	0.400	7.300	12.800	11.400	0.900	6.600	5.075
Sr	2.400	1.400	1.400	2.000	8.200	13.600	8.300	1.900	4.900
U	0.610	0.490	0.320	0.220	0.140	0.090	0.080	2.720	0.584
Th	0.350	0.270	0.360	0.290	0.220	0.250	0.250	2.010	0.500
Pb	14.000	12.000	8.000	10.000	9.000	9.000	10.000	22.000	11.750
Zr	17.000	7.000	5.000	8.000	6.000	5.000	3.000	13.000	8.000
Y	28.700	0.700	2.300	1.900	20.600	4.600	5.300	10.500	9.325
W	0.700	0.700	0.500	0.500	<dl	<dl	<dl	<dl	0.300
La	4.800	2.100	1.900	1.500	12.600	2.700	8.300	5.400	4.913
Ce	6.300	8.200	2.800	3.300	26.500	5.900	14.800	7.400	9.400
Pr	0.930	0.310	0.440	0.360	2.630	0.720	1.720	1.550	1.083
Nd	4.400	0.900	1.900	1.400	11.100	3.200	6.800	5.900	4.450
Sm	1.220	0.180	0.570	0.380	2.360	0.790	1.040	1.800	1.043
Eu	0.690	0.050	0.160	0.130	1.060	0.320	0.560	0.500	0.434
Gd	2.260	0.190	0.580	0.400	2.960	0.770	0.980	1.720	1.233
Tb	0.420	0.030	0.120	0.070	0.430	0.120	0.130	0.310	0.204
Dy	3.350	0.160	0.670	0.460	2.830	0.720	0.900	2.190	1.410
Ho	0.880	0.030	0.150	0.100	0.580	0.140	0.190	0.480	0.319
Er	2.910	0.080	0.480	0.300	1.860	0.480	0.580	1.400	1.011
Tm	0.440	0.020	0.070	0.030	0.210	0.060	0.080	0.230	0.143
Yb	2.910	0.130	0.560	0.350	1.220	0.310	0.570	1.580	0.954
Lu	0.490	0.020	0.090	0.040	0.200	0.040	0.090	0.220	0.149
Y/P_2O_5	29.896	7.000	32.857	9.500	206.000	41.818	66.250	21.429	51.844
Co/Zn	0.089	0.091	0.143	0.148	0.170	0.070	0.200	0.146	0.132
Eu/Sm	0.566	0.278	0.281	0.342	0.449	0.405	0.538	0.278	0.392
Y/Ho	32.614	23.333	15.333	19.000	35.517	32.857	27.895	21.875	26.053
$(La/Yb)_{SN}$	1.649	16.154	3.393	4.286	10.328	8.710	14.561	3.418	7.812
$(Tb/Yb)_{SN}$	0.526	0.841	0.781	0.729	1.284	1.410	0.831	0.715	0.890
$(La/Yb)_{CN}$	1.115	10.920	2.293	2.897	6.979	5.886	9.842	2.310	5.280
$(Tb/Yb)_{CN}$	0.617	0.987	0.916	0.855	1.507	1.655	0.975	0.839	1.044
$(Eu/Eu^*)_{CN}$	1.871	0.462	0.892	0.822	0.751	0.657	0.613	0.849	0.865
$(Eu/Eu^*)_{SN}$	1.957	1.273	1.310	1.570	1.889	1.932	2.612	1.338	1.735
$(Pr/Pr^*)_{SN}$	1.039	0.671	1.122	0.985	0.902	0.975	1.009	1.380	1.010
$(Ce/Ce^*)_{SN}$	0.638	2.173	0.655	0.960	0.984	0.905	0.837	0.547	0.962
∑REE	32.000	12.400	10.490	8.820	66.540	16.270	36.740	30.680	26.743

dl: detection limits. $(Ce/Ce^*)_{SN}$ = (Ce rock/Ce PAAS)/[(La rock/La PAAS)0.5(Pr rock/Pr PAAS)0.5]; $(Eu/Eu^*)_{SN}$ = (Eu rock/Eu PAAS)/[(Sm rock/Sm PAAS)0.5(Gd rock/Gd PAAS)0.5]; $(La/Yb)_{SN}$ = (La rock/La PASS)/(Yb rock/Yb PASS); $(Tb/Yb)_{SN}$ = (Tb rock/Yb PASS)/(Yb rock/Yb PASS); $(Pr/Pr^*)_{SN}$ = (Pr rock/Pr PAAS)/[(Ce rock/Ce PAAS)0.5(Nd rock/Nd PAAS)0.5].

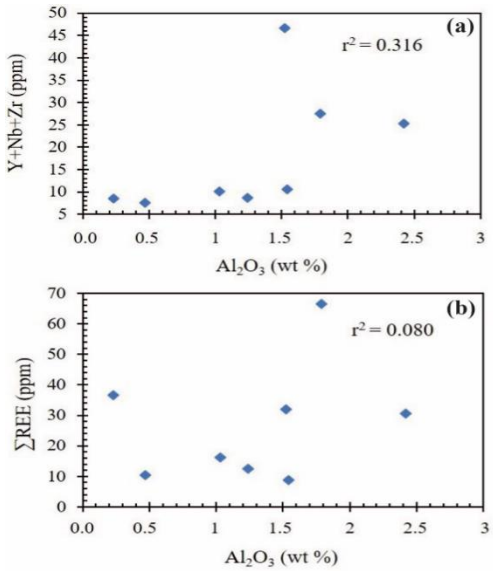

Fig. 8: (A) - Detrital Trace Elements (Nb, Y, And Zr) vs. Al_2O_3 Showing Relatively Low Positive Correlations Between Al_2O_3 and These Elements; (B) - Null Correlations Between Al_2O_3 and the ∑REE in the Bulk Samples of the Studied BIF.

5.2. Origin of Mingo'o BIF

The degassing of submarine hydrothermal fluids and the weathering of continental crustal materials combine to produce Fe- and Si-rich BIFs [52]. The approaches that have been put out to make the distinction between seawater sources that are hydrothermal, biogenic, and detrital depend on variations in the composition of minerals, chemicals, and isotopes. For instance, Al^{3+} and Ti^{4+} are considered to be very insoluble in seawater and resistant to hydrothermal alteration [53], [54]. Hydrothermal fluids present high ratios of Fe/Ti, Fe/Al, and Si/Al (Table 1) as a consequence. The Mingo'o BIFs have high ratios of Fe/Ti (3312.10), Fe/Al (104.75), and Si/Al (44.07) that are indicative of sediments that have significant levels of hydrothermal process [54] or that originated from oceanic crust or Fe- and Si-rich submarine weathered shales where Ti and Al form a solid solution in a mineral phase.

The depiction in the hydrothermal field of [55] Si-Al discrimination diagram (Fig. 9a) confirms that the origin of the BIFs studied is mostly hydrothermal. High Al/Ti ratios and low Al content are characteristics of pure hydrothermal deposits [56]. Deep-sea pelagic and terrigenous sediments contaminate these deposits, enriching them with elements like Ti and Al. This causes a sharp decrease in the Fe/Ti ratios and an increase in the Al/(Al + Fe + Mn) ratio. When considering the potential hydrothermal input in hydrogenated sediments and their dilution with clastic or volcanic material, the Fe/Ti vs. Al/(Al + Fe + Mn) diagram is helpful [57–59]. According to [60], the diagram illustrates that clastic or volcanic material is defined by Al and Ti, whereas pure hydrothermal chemical sediments are rich in Fe and Mn. As can be observed in the diagram, all of the samples studied were centered on the hydrothermal deposits of the Red Sea and the East Pacific Rise (13°N and 21°N), which are situated far from the contemporary pelagic-terrigenous sediments (Fig. 9b). This implies that the majority of the Mingo'o BIF's constituents (>90%) are primarily hydrothermally derived. A low average Y/P_2O_5 ratio of 51.84, which is less than the >100 found in pelagic and hydrogenated deposits but comparable to ratios indicated in pure hydrothermal deposits, is likewise compatible with a mostly hydrothermal origin (Table 3; [56]). With the exception of sample MIN12, which indicates a hydrogenated origin with a Y/P_2O_5 ratio of 206, which is greater than 100 (Table 3). The prior conclusion that the BIFs studied are purely chemical sediments with little or no detrital input is confirmed by the low levels of detrital elements like Y, Nb, and Zr in the Mingo'o BIF and the low positive correlations between Al_2O_3 and these elements (Fig. 8a). This conclusion was based on the major oxide distributions. Furthermore, there appears to be no detrital contribution to the ∑REE contents, as indicated by the zero correlations ($r^2 = 0.08$) between the ∑REE contents and the Al_2O_3 contents (Fig. 8b).

[61] suggested using the Co/Zn ratio as a hydrothermal input tracer. This author affirms that hydrothermal deposits have a low Co/Zn ratio (0.15), while hydrogen deposits have a high Co/Zn ratio (2.5). The iron mineralization samples studied had an average Co/Zn ratio of 0.13, which is in line with trace metals coming mostly from hydrothermal sources with a little proportion of hydrogen impact (Table 3; [61]). Therefore, hydrothermal solutions, which could have originated from hydrothermal vents in marine environments, added the materials that form the mineralization to the seafloor.

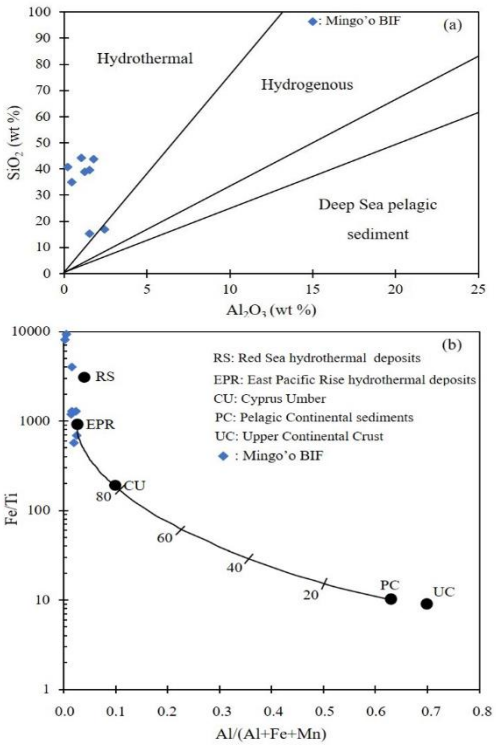

Fig. 9: (A) - Si Vs. Al Discrimination Diagram Indicating the Hydrothermal Affinity of the Studied BIF; (B) - Fe/Ti Vs. Al/(Al + Fe + Mn) Diagram of Mingo'o BIF. the Curve Represents Mixing of East Pacific Rise Deposits (EPR) with Pelagic Sediments (PC) Whereas the Numbers Indicate the Approximate Percentage of EPR in the Mixture (Adopted From [57]). Also Indicated Are Compositions for Mean Upper Continental Crust (UC, [38]), Red Sea Hydrothermal Deposits (RS, [56]) And The Cyprus Umber (CU).

5.3. Petrography and geochemistry in comparison

According to [39], [62–64], the mineral assemblages presented in the petrographic section are similar to oxidized facies banded iron formations found all over the world. The majority of BIFs in Cameroon are oxide facies, with magnetite or hematite predominating. The Mingo'o BIFs are mostly magnetite-rich, similar to the Ngoa and Elom iron ore deposits, when compared to other BIF occurrences in the same Precambrian iron ore belt in southern Cameroon [15]. The iron ore deposits in Metzimevin, Njweng (Mballam), and Nkout are not the same as these iron mineralizations in Mingo'o; the former are mostly made of hematite and martite, with minor phases of monazite, apatite, and pyrite [21], [65]. Furthermore, the silicate facies BIF in the Njweng prospect of the Mballam iron ore deposit was characterized by [65]. The Mingo'o region has not seen any of these BIF varieties. When compared to the average chemical compositions of other banded iron formations found in the Proterozoic and Archean supracrustal belts, the Mingo'o banded iron formations have slightly elevated Fe_2O_3 values and depressed SiO_2, TiO_2, MgO, MnO, CaO, Na_2O, K_2O, and P_2O_5 values in bulk rock geochemistry (Fig. 10a). The proportions of MnO, which are extremely low in the BIF of the study area, vary significantly, as seen in this Figure, although the proportions of Fe_2O_3 are slightly higher. The average P_2O_5 concentration (0.3 wt. %) in the BIFs studied is greater than the one in Isua (0.2 wt. %), Hamersley (0.15 wt. %), Hotazel (0.12 wt. %), Orissa (0.06 wt. %), and Superior (0.04 wt. %) types, but it is similar to that of the Algoma oxidized facies [63]. According to [66], the Al_2O_3 concentrations of the Mingo'o BIF (1.5 wt. %) are high in comparison to the Al_2O_3 contents of the Orissa BIF (0.8 wt. %), which are close to the Al_2O_3 concentrations of the Isua and Superior BIF (1.6 wt. %). There are various concentrations of iron-rich silicate minerals found inside the different banded iron formations, as shown by the slight variations in Al_2O_3, K_2O, and Na_2O_3. The metal concentrations of the Algoma, Superior, Isua, Hamersley, and Hotazel types are similar to the Zn Cu, Ni Co, and V contents of the BIFs studied, with values >2 ppm (Fig. 10b). With a mean REE concentration ($\sum$REE = 26.74 ppm) comparable to other Archean to Proterozoic oxide-facies BIFs around the world, the REE depletion of the Mingo'o BIFs is compatible with REE data from Archean iron formations elsewhere [39], [67]. Similar to REE profiles from other Archean BIFs [15,20,50,68], PASS-normalized REE profiles from the study area show slightly positive Eu anomalies (Eu/Eu* = 1.73) relative to HREE (Tb_{SN}/Yb_{SN} = 0.89) with slightly negative Ce anomalies (Ce/Ce* = 0.96). Archean, early (> 2.4 Ga) and late (< 2.0 Ga) Palaeoproterozoic banded iron formations are characterized by negative Ce anomalies [20], [67]. Due to their low positive Eu anomalies, which are comparable to those of late Palaeoproterozoic BIFs, we consequently suggest that the Mingo'o BIFs were most likely deposited between the early and late Palaeoproterozoic [67]. Moreover, [68] proposed that Archean (0.40-1.22) and Proterozoic (0.24-0.40) BIF may be distinguished using the Eu/Sm ratio. Between 0.27 and 0.56 is the Eu/Sm ratio of the BIFs studied, which includes both Archean and Proterozoic BIFs.

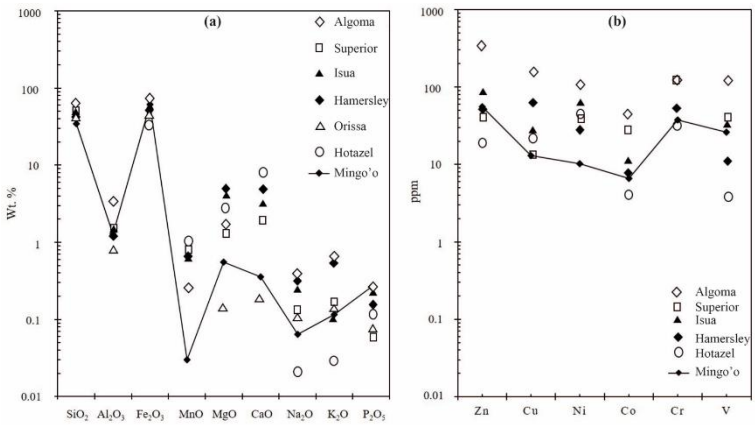

Fig. 10: Plot of Average Major Elements Concentrations (A) and Transition Metal Values (B) of Mingo'o BIF (N = 8) and Other Well Studied Banded Iron-Formations Around the World.

6. Conclusion

To understand the origins of the Fe formations, representative samples of BIFs from the Mingo'o region in the Ntem complex (southern Cameroon) were analyzed for their major, trace, and rare earth elements. The BIFs studied are mostly oxide facies comprised of potassic felspar, microcrystalline quartz, and magnetite. The majority of the BIF samples have low concentrations of Al_2O_3, TiO_2, Y, Nb, Zr, and Th, indicating chemical sediments lacking detritus. The BIFs studied have an average Si/Al ratio (mean 44.07), which points to a hydrothermal origin. This hypothesis is confirmed by the Fe/Ti vs. Al/(Al + Fe + Mn) binary diagram, which plots all the data in the Red Sea and East Pacific Rise hydrothermal deposit fields (Fig. 9b). Conversely, the low ∑REE concentrations, the Y/Ho ratio nearby chondrules, and the HREE profiles for the BIFs studied reveal the signs of seawater and hydrothermal solutions. A positive Eu anomaly is an indicator obtained from bottom water carrying a hydrothermal signature, whereas HREE enrichment is a signature inherited from seawater. Low-temperature hydrothermal solutions play a key role in the BIF studied, as evidenced by the lack of a strong positive Eu anomaly. It is possible that the Mingo'o BIFs were precipitated in suboxic to anoxic seawater since negative Ce anomalies were found in the samples studied. According to [67], this suggests that the redox conditions in the Mingo'o basin were variable, possibly in a stratified basin with a redoxcline dividing the deeper anoxic to suboxic waters from the upper oxic water column. Deposition possibly occurred in places of the basin towards redoxcline, alternating at different times and under various influences from the influx of seawater that has been oxidized.

Acknowledgements

The authors are grateful to the School of Geology and Mining Engineering (University of Ngaoundere, Cameroon) for providing polarizing microscopy useful for this work. The authors also thank the Ore Processing Laboratory of the Institute for Geological and Mining Research (Cameroon) for thin section analysis. A great acknowledgement goes to ALS Global, Brisbane (Australia), which has done all the geochemistry analysis for this work. Thank you to Professor John Ayila, Divine Nji Tandong, Madi Boukar, Kevin Otiti, Thierry Molo, Claude Lionel Mvondo, William Gaspard Manga Owona, Nadege Essoh, and Oliselle Fogang for their advice during the realization of this work. Finally, the authors thank the anonymous reviewers which improve the quality of the manuscript.

References

[1] M.M. Kimberley, Exhalative origins of iron formations, Ore Geology Reviews 5 (1989) 13–145. https://doi.org/10.1016/0169-1368(89)90003-6.
[2] M.M. Kimberley, Paleoenvironmental classification of iron formations, Economic Geology 73 (1978) 215–229. https://doi.org/10.2113/gsecongeo.73.2.215.
[3] A. Bekker, B. Krapez, J.F. Slack, N. Planavsky, A. Hofmann, K.O. Konhauser, O.J. Rouxel, Iron Formation: the Sedimentary Product of a Complex Interplay among Mantle, Tectonic, Oceanic, and Biospheric processes--a reply, Economic Geology 107 (2012) 379–380. https://doi.org/10.2113/econgeo.107.2.379.
[4] G.A. Gross, A classification of iron formations based on depositional environments, The Canadian Mineralogist 18 (1980) 215–222.
[5] P. Cloud, Paleoecological Significance of the Banded Iron-Formation, Economic Geology 68 (1973) 1135–1143. https://doi.org/10.2113/gsecongeo.68.7.1135.
[6] M. Zhai, T.-S. Li, P. Peng, B. Hu, F. Liu, Y. Zhang, Precambrian key tectonic events and evolution of the North China craton., Geological Society, London, Specail Publication 338 (2010) 235–262. https://doi.org/10.1144/SP338.12.
[7] L. Zhang, M. Zhai, X. Zhang, P. Xiang, Y. Dai, C. Wang, F. Pirajno, Formation age and tectonic setting of the Shirengou Neoarchean banded iron deposit in eastern Hebei Province: Constraints from geochemistry and SIMS zircon U–Pb dating, Precambrian Research 222–223 (2012) 325–338. https://doi.org/10.1016/j.precamres.2011.09.007.
[8] E.R. Ramanaidou, M.A. Wells, Sedimentary Hosted Iron Ores, in: Treatise on Geochemistry, Elsevier, 2014: pp. 313–355. https://doi.org/10.1016/B978-0-08-095975-7.01115-3.
[9] N.J. Beukes, J. Gutzmer, Origin and Paleoenvironmental Significance of Major Iron Formations at the Archean-Paleoproterozoic Boundary, in: Banded Iron Formation-Related High-Grade Iron Ore, Society of Economic Geologists 15 (2008) 5–47. https://doi.org/10.5382/Rev.15.01.
[10] M. Flis, Advances in Geophysics Applied to the Search for Banded Iron Formation-Related, High-Grade Hematite Iron Ore, in: S. Hagemann, C.A. Rosière, J. Gutzmer, N.J. Beukes (Eds.), Banded Iron Formation-Related High-Grade Iron Ore, Society of Economic Geologists 15 (2008), p. 0. https://doi.org/10.5382/Rev.15.15.
[11] S.G. Hagemann, T. Angerer, P. Duuring, C.A. Rosière, R.C. Figueiredo e Silva, L. Lobato, A.S. Hensler, D.H.G. Walde, BIF-hosted iron mineral system: A review, Ore Geology Reviews 76 (2016) 317–359. https://doi.org/10.1016/j.oregeorev.2015.11.004.
[12] A.T. Melo, J. Sun, Y. Li, Geophysical inversions applied to 3D geology characterization of an iron oxide copper-gold deposit in Brazil, Geophysics 82 (2017) K1–K13. https://doi.org/10.1190/geo2016-0490.1.

[13] S. Ganno, D. Tsozué, G.D. Kouankap Nono, M.S. Tchouatcha, T. Ngnotué, R. Gamgne Takam, J.P. Nzenti, Geochemical Constraints on the Origin of Banded Iron Formation-Hosted Iron Ore from the Archaean Ntem Complex (Congo Craton) in the Meyomessi Area, Southern Cameroon: Geochemistry of the Meyomessi BIF, Resource Geology 68 (2018) 287–302. https://doi.org/10.1111/rge.12172.

[14] S. Ganno, C. Moudioh, A. Nzina Nchare, G.D. Kouankap Nono, J.P. Nzenti, Geochemical fingerprint and iron ore potential of the siliceous itabirite from Palaeoproterozoic Nyong Series, Zambi area, Southwestern Cameroon, Resource Geology 66 (2016) 71–80. https://doi.org/10.1111/rge.12081.

[15] S. Ganno, T. Ngnotue, K.G.D. Nono, J.P. Nzenti, N.M. Fokeng, Petrology and geochemistry of the banded iron-formations from Ntem complex greenstones belt, Elom area, Southern Cameroon: Implications for the origin and depositional environment, Geochemistry 75 (2015) 375–387. https://doi.org/10.1016/j.chemer.2015.08.001.

[16] E.N. Ndime, S. Ganno, L. Soh Tamehe, J.P. Nzenti, Petrography, lithostratigraphy and major element geochemistry of Mesoarchean metamorphosed banded iron formation-hosted Nkout iron ore deposit, north western Congo craton, Central West Africa, Journal of African Earth Sciences 148 (2018) 80–98. https://doi.org/10.1016/j.jafrearsci.2018.06.007.

[17] G.N. Ngoran, C.E. Suh, D. Bowker, R.B. Verla, G.T. Bafon, Petrochemistry of Two Magnetite Bearing Systems in the Precambrian Belt of Southern Cameroon, International Journal of Geosciences 7 (2016) 501–517. https://doi.org/10.4236/ijg.2016.74038.

[18] L. Soh Tamehe, W. Chongtao, S. Ganno, R. Carlos Alberto, J.P. Nzenti, C.G. Ebotehouna, L. Guanwen, Depositional age and tectonic environment of the Gouap banded iron formations from the Nyong group, SW Cameroon: Insights from isotopic, geochemical and geochronological studies of drillcore samples, Geoscience Frontiers 12 (2021) 549–572. https://doi.org/10.1016/j.gsf.2020.07.009.

[19] L. Soh Tamehe, C. Wei, S. Ganno, S.J. Simon, G.K.N. Djibril, N. Jean Paul, B.L. Yanick, N.H. Lin, Geology of the Gouap iron deposit, Congo craton, southern Cameroon: Implications for iron ore exploration, Ore Geology Reviews 107 (2019) 1097–1128. https://doi.org/10.1016/j.oregeorev.2019.03.034.

[20] L. Soh Tamehe, T. Nzepang, W. Chongtao, S. Ganno, T. Ngnotue, G.D. Kouankap Nono, S.J. Shaamu, Z. Junjian, J.P. Nzenti, Geology and geochemical constrains on the origin and depositional setting of the Kpwa–Atog Boga banded iron formations (BIFs), northwestern Congo craton, southern Cameroon, Ore Geology Reviews 95 (2018) 620–638. https://doi.org/10.1016/j.oregeorev.2018.03.017.

[21] C.E. Suh, A.R. Cabral, E.M. Shemang, L. Mbinkar, G.G.M. Mboudou, Two Contrasting Iron Deposits in the Precambrian Mineral Belt of Cameroon, West Africa, Exploration and Mining Geology 17 (2008) 197–207. https://doi.org/10.2113/gsemg.17.3-4.197.

[22] T. Teutsong, T.R.R. Bontognali, P.-D. Ndjigui, J.C. Vrijmoed, D. Teagle, M. Cooper, D. Vance, Petrography and geochemistry of the Mesoarchean Bikoula banded iron formation in the Ntem complex (Congo craton), Southern Cameroon: Implications for its origin, Ore Geology Reviews 80 (2017) 267–288. https://doi.org/10.1016/j.oregeorev.2016.07.003.

[23] P. Maurizot, A. Abessolo, J.L. Feybesse, V. Joyan, P. Lecomte, Etude et prospection minière du Sud-Ouest Cameroun synthèse des travaux de 1978 à 1985, Rapport du BRGM n 85. (1986).

[24] A. Nédélec, E.N. Nsifa, H. Martin, Major and trace element geochemistry of the Archaean Ntem plutonic complex (south Cameroon): petrogenesis and crustal evolution, Precambrian Research 47 (1990) 35–50. https://doi.org/10.1016/0301-9268(90)90029-P.

[25] J.P. Nzenti, P. Barbey, J. Macaudiere, D. Soba, Origin and evolution of the late precambrian high-grade Yaounde Gneisses (Cameroon), Precambrian Research 38 (1988) 91–109. https://doi.org/10.1016/0301-9268(88)90086-1.

[26] R. Tchameni, K. Mezger, N.E. Nsifa, A. Pouclet, Crustal origin of Early Proterozoic syenites in the Congo Craton Ntem Complex, South Cameroon, Lithos 57 (2001) 23–42. https://doi.org/10.1016/S0024-4937(00)00072-4.

[27] A. Pouclet, R. Tchameni, M. Klaus, M. Vidal, E. Nsifa, C. Shang, J. Penaye, Archaean crustal accretion at the northern border of the Congo Craton (South Cameroon). The charnockite-TTG link, Bulletin de La Société Géologique de France 178 (2007) 331–342. https://doi.org/10.2113/gssgfbull.178.5.331.

[28] T. Takam, M. Arima, K. Joseph, D.J. Daniel, N.N. Emmanuel, Paleoarchaean charnockite in the Ntem Complex, Congo Craton, Cameroon: insights from SHRIMP zircon U-Pb ages, Journal of Mineralogical and Petrological Sciences 104 (2009) 1–11. https://doi.org/10.2465/jmps.080624.

[29] R. Tchameni, C. Lerouge, J. Penaye, A. Cocherie, J.P. Milesi, S.F. Toteu, N.E. Nsifa, Mineralogical constraint for metamorphic conditions in a shear zone affecting the Archean Ngoulemakong tonalite, Congo craton (Southern Cameroon) and retentivity of U–Pb SHRIMP zircon dates, Journal of African Earth Sciences 58 (2010) 67–80. https://doi.org/10.1016/j.jafrearsci.2010.01.009.

[30] R. Tchameni, Monozircon and Sm-Nd whole rock ages from the Ebolowa greenstone belts : Evidence for the terranes older than 2.9 Ga in the Ntem Complex (Congo craton, South Cameroon), Journal of Cameroon Academic Sciences 4 (2004) 213–224.

[31] C. Lerouge, A. Cocherie, S.F. Toteu, J. Penaye, J.-P. Milési, R. Tchameni, E.N. Nsifa, C. Mark Fanning, E. Deloule, Shrimp U–Pb zircon age evidence for Paleoproterozoic sedimentation and 2.05Ga syntectonic plutonism in the Nyong Group, South-Western Cameroon: consequences for the Eburnean–Transamazonian belt of NE Brazil and Central Africa, Journal of African Earth Sciences 44 (2006) 413–427. https://doi.org/10.1016/j.jafrearsci.2005.11.010.

[32] J. Penaye, F.S. Toteu, R. Tchameni, W.R. Van Schmus, J. Tchakounté, A. Ganwa, D. Minyem, E.N. Nsifa, The 2.1Ga West Central African Belt in Cameroon: extension and evolution, Journal of African Earth Sciences 39 (2004) 159–164. https://doi.org/10.1016/j.jafrearsci.2004.07.053.

[33] S.F. Toteu, W.R. Van Schmus, J. Penaye, J.B. Nyobé, U-Pb and Sm-Nd evidence for Eburnian and Pan-African high-grade metamorphism in cratonic rocks of southern Cameroon, Precambrian Research 67 (1993) 321–347. https://doi.org/10.1016/0301-9268(94)90014-0.

[34] H. Bouyo, J. Penaye, H. Mouri, F.S. Toteu, Eclogite facies metabasites from the Paleoproterozoic Nyong Group, SW Cameroon: Mineralogical evidence and implications for a high-pressure metamorphism related to a subduction zone at the NW margin of the Archean Congo craton, Journal of African Earth Sciences 149 (2019) 215–234. https://doi.org/10.1016/j.jafrearsci.2018.08.010.

[35] Loose, V. Schenk, 2.09 Ga old eclogites in the Eburnian-Transamazonian orogen of southern Cameroon: Significance for Palaeoproterozoic plate tectonics, Precambrian Research 304 (2018) 1–11. https://doi.org/10.1016/j.precamres.2017.10.018.

[36] M. Houketchang Bouyo, J. Penaye, H. Mouri, S.F. Toteu, Eclogite facies metabasites from the Paleoproterozoic Nyong Group, SW Cameroon: Mineralogical evidence and implications for a high-pressure metamorphism related to a subduction zone at the NW margin of the Archean Congo craton, Journal of African Earth Sciences 149 (2019) 215–234. https://doi.org/10.1016/j.jafrearsci.2018.08.010.

[37] S.M. McLennan, Rare earth elements in sedimentary rocks: influence of provenance and sedimentary processes, Reviews in Mineralogy and Geochemistry (1989) 169–200. https://doi.org/10.1515/9781501509032-010.

[38] S.R. Taylor, S.M. McLennan, The continental crust: Its composition and evolution, Blackwell Publishing (1985) 312.

[39] C. Klein, Some Precambrian banded iron-formations (BIFs) from around the world: Their age, geologic setting, mineralogy, metamorphism, geochemistry, and origins, American Mineralogist 90 (2005) 1473–1499. https://doi.org/10.2138/am.2005.1871.

[40] F.F. Basta, A.E. Maurice, L. Fontboté, P.-Y. Favarger, Petrology and geochemistry of the banded iron formation (BIF) of Wadi Karim and Um Anab, Eastern Desert, Egypt: Implications for the origin of Neoproterozoic BIF, Precambrian Research 187 (2011) 277–292. https://doi.org/10.1016/j.precamres.2011.03.011.

[41] E. Pecoits, M.K. Gingras, M.E. Barley, A. Kappler, N.R. Posth, K.O. Konhauser, Petrography and geochemistry of the Dales Gorge banded iron formation: Paragenetic sequence, source and implications for palaeo-ocean chemistry, Precambrian Research 172 (2009) 163–187. https://doi.org/10.1016/j.precamres.2009.03.014.

[42] T. Gnaneshwar Rao, S.M. Naqvi, Geochemistry, depositional environment and tectonic setting of the BIF's of the Late Archaean Chitradurga Schist Belt, India, Chemical Geology 121 (1995) 217–243. https://doi.org/10.1016/0009-2541(94)00116-P.

[43] P.V. Sunder Raju, Petrography and geochemical behaviour of trace element, REE and precious metal signatures of sulphidic banded iron formations from the Chikkasiddavanahalli area, Chitradurga schist belt, India, Journal of Asian Earth Sciences 34 (2009) 663–673. https://doi.org/10.1016/j.jseaes.2008.10.005.

[44] A.M. Mloszewska, E. Pecoits, N.L. Cates, S.J. Mojzsis, J. O'Neil, L.J. Robbins, K.O. Konhauser, The composition of Earth's oldest iron formations: The Nuvvuagittuq Supracrustal Belt (Québec, Canada), Earth and Planetary Science Letters 317–318 (2012) 331–342. https://doi.org/10.1016/j.epsl.2011.11.020.

[45] M. Bau, P. Dulski, Distribution of yttrium and rare-earth elements in the Penge and Kuruman iron-formations, Transvaal Supergroup, South Africa, Precambrian Research 79 (1996) 37–55. https://doi.org/10.1016/0301-9268(95)00087-9.
[46] H.D. Holland, The Oceans; A Possible Source of Iron in Iron-Formations, Economic Geology 68 (1973) 1169–1172. https://doi.org/10.2113/gsecongeo.68.7.1169.
[47] D.L. Huston, G.A. Logan, Barite, BIFs and bugs: evidence for the evolution of the Earth's early hydrosphere, Earth and Planetary Science Letters 220 (2004) 41–55. https://doi.org/10.1016/S0012-821X(04)00034-2.
[48] A. Danielson, P. Möller, P. Dulski, The europium anomalies in banded iron formations and the thermal history of the oceanic crust, Chemical Geology 97 (1992) 89–100. https://doi.org/10.1016/0009-2541(92)90137-T.
[49] T.-G. Lan, H.-R. Fan, F.-F. Hu, K.-F. Yang, Y.-C. Cai, Y.-S. Liu, Depositional environment and tectonic implications of the Paleoproterozoic BIF in Changyi area, eastern North China Craton: Evidence from geochronology and geochemistry of the metamorphic wallrocks, Ore Geology Reviews 61 (2014) 52–72. https://doi.org/10.1016/j.oregeorev.2014.01.007.
[50] C. Klein, N.J. Beukes, Sedimentology and geochemistry of the glaciogenic late Proterozoic Rapitan Iron-Formation in Canada, Economic Geology 88 (1993) 542–565. https://doi.org/10.2113/gsecongeo.88.3.542.
[51] C. Manikyamba, S.M. Naqvi, Geochemistry of Fe-Mn formations of the Archaean Sandur schist belt, India - mixing of clastic and chemical processes at a shallow shelf, Precambrian Research 72 (1995) 69–95. https://doi.org/10.1016/0301-9268(94)00050-2.
[52] Ya.N. Belevtsev, Volcanogenic-sedimentary origin of magnetite ores of the Urals, International Geology Review 24 (1982) 1405–1416. https://doi.org/10.1080/00206818209467200.
[53] K. Boström, Submarine volcanism as a source for iron, Earth and Planetary Science Letters 9 (1970) 348–354. https://doi.org/10.1016/0012-821X(70)90134-2.
[54] E.G. Gurvich, Metalliferous sediments of the world ocean: Fundamental theory of deep-sea hydrothermal sedimentation, Metalliferous Sediments of the World Ocean: Fundamental Theory of Deep-Sea Hydrothermal Sedimentation (2006) 200–300. https://doi.org/10.1007/3-540-30969-1.
[55] J.H. Choi, Y. Hariya, Geochemistry and depositional environment of Mn oxide deposits in the Tokoro Belt, northeastern Hokkaido, Japan, Economic Geology 87 (1992) 1265–1274. https://doi.org/10.2113/gsecongeo.87.5.1265.
[56] V. Marchig, H. Gundlach, Iron-rich metalliferous sediments on the East Pacific Rise: prototype of undifferentiated metalliferous sediments on divergent plate boundaries, Earth and Planetary Science Letters 58 (1982) 361–382. https://doi.org/10.1016/0012-821X(82)90086-3.
[57] T.J. Barrett, Chemistry and mineralogy of Jurassic bedded chert overlying ophiolites in the North Apennines, Italy, Chemical Geology 34 (1981) 289–317. https://doi.org/10.1016/0009-2541(81)90118-2.
[58] K. Boström, Origin and Fate of Ferromanganoan Active Ridge Sediments, in: Pelagic Sediments: On Land and under the Sea, John Wiley & Sons, Ltd, 1975: pp. 149–243. https://doi.org/10.1002/9781444304855.ch18.
[59] K. Boström, T. Kraemer, S. Gartner, Provenance and accumulation rates of opaline silica, Al, Ti, Fe, Mn, Cu, Ni and Co in Pacific pelagic sediments, Chemical Geology 11 (1973) 123–148. https://doi.org/10.1016/0009-2541(73)90049-1.
[60] P.D. González, A.M. Sato, E.J. Llambías, L.A. Petronilho, Petrology and geochemistry of the banded iron formation in the Eastern Sierras Pampeanas of San Luis (Argentina): Implications for the evolution of the Nogolí Metamorphic Complex, Journal of South American Earth Sciences 28 (2009) 89–112. https://doi.org/10.1016/j.jsames.2009.03.005.
[61] J.R. Toth, Deposition of submarine crusts rich in manganese and iron, GSA Bulletin 91 (1980) 44–54. https://doi.org/10.1130/0016-7606(1980)91<44:DOSCRI>2.0.CO;2. https://doi.org/10.1130/0016-7606(1980)91<44:DOSCRI>2.0.CO;2.
[62] N.J. Beukes, Precambrian Iron-Formations of Southern Africa, Economic Geology 68 (1973) 960–1004. https://doi.org/10.2113/gsecongeo.68.7.960.
[63] H.N. Bhattacharya, I. Chakraborty, K.K. Ghosh, Geochemistry of some banded iron-formations of the Archean supracrustals, Jharkhand-Orissa region, India, J Earth Syst Sci 116 (2007) 245–259. https://doi.org/10.1007/s12040-007-0024-4.
[64] H.L. James, Sedimentary facies of iron-formation, Economic Geology 49 (1954) 235–293. https://doi.org/10.2113/gsecongeo.49.3.235.
[65] D.C.I. Ilouga, C.E. Suh, G.R. Tanwi, Textures and Rare Earth Elements Composition of Banded Iron Formations (BIF) at Njweng Prospect, Mbalam Iron Ore District, Southern Cameroon, IJG 04 (2013) 146–165. https://doi.org/10.4236/ijg.2013.41014.
[66] H. Tsikos, J.M. Moore, Petrography and geochemistry of the Paleoproterozoic Hotazel Iron-Formation, Kalahari manganese field, South Africa; implications for Precambrian manganese metallogenesis, Economic Geology 92 (1997) 87–97. https://doi.org/10.2113/gsecongeo.92.1.87.
[67] N. Planavsky, A. Bekker, O.J. Rouxel, B. Kamber, A. Hofmann, A. Knudsen, T.W. Lyons, Rare Earth Element and yttrium compositions of Archean and Paleoproterozoic Fe formations revisited: New perspectives on the significance and mechanisms of deposition, Geochimica et Cosmochimica Acta 74 (2010) 6387–6405. https://doi.org/10.1016/j.gca.2010.07.021.
[68] B.J. Fryer, Rare earth evidence in iron-formations for changing Precambrian oxidation states, Geochimica et Cosmochimica Acta 41 (1977) 361–367. https://doi.org/10.1016/0016-7037(77)90263-0.